Defence Science Journal, Vol. 73, No. 1, January 2023, pp. 29-40, DOI : 10.14429/dsj.73.1.17828

Design and Performance Analysis of a Switched Reluctance Motor Using Finite Element Analysis and Magnetic Equivalent Circuit Model

Sandesh Bhaktha B., Satish Kumawat, Jeyaraj Pitchaimani and K.V. Gangadharan*

Department of Mechanical Engineering, National Institute of Technology Karnataka, Surathkal, Mangalore – 575 025, India

**E-mail: kvganga@gmail.com*

ABSTRACT

By being magnet-free, and mechanically robust with a longer constant power range, switched reluctance motor (SRM) is gathering much attention as a potential choice to propel electric vehicles (EVs) and hybrid electric vehicles (HEVs). This paper comprehensively investigates the performance sensitivity to geometric design variables such as rotor diameter, pole arc angles, and yoke thicknesses for an SRM using static two-dimensional (2D) electromagnetic Finite-Element Analysis (FEA). The reason for the change in static characteristics due to variation in reluctance between SRM designs has not been detailed previously. This is addressed by the magnetic equivalent circuit (MEC) model that simplifies the design analysis. Results indicate that stator pole reluctance needs to be given due importance while studying the influence of rotor diameter. Also, it is imperative to set an adequate thickness of the stator and rotor yokes to minimize the effect of saturation on the performance. Rotor diameter and stator pole arc angle have a pronounced influence on the performance while the influence of rotor pole arc angle and yoke thicknesses was relatively less.

Keywords: Electric vehicles; Switched reluctance motor; Finite-element analysis; Magnetic equivalent circuit; Performance indicators

1. INTRODUCTION

The ever-increasing demand for global crude oil against the backdrop of depleting natural resources coupled with an increased global carbon footprint has led governments across the world to look for alternative environment-friendly means of mobility to meet their demands[1-2]. Amongst the available traction motors, switched reluctance motors are a promising candidate for application in EVs and HEVs. Besides their superior performance, they are a cost-effective alternative since they do not employ permanent magnets[3]. Moreover, they showcase a longer constant power region making it a promising alternative for EV applications[4]. However, high torque ripples causing abnormal noise and vibrations have proven to be a major hindrance to its wide-scale use[5]. Despite these drawbacks, studies have successfully demonstrated its potential as a promising traction motor in the commercial arena[6-7].

SRM assembly primarily comprises salient poles both on the stator and rotor cores made up of electrical steel lamination sheets. Diametrically opposite stator poles with mounted concentrated windings connected in parallel or series form a phase. On energising a suitable stator phase, the rotor pole tends to orient itself into a state of the maximum inductance of the corresponding phase, thus generating torque. To attain continuous rotation, the stator phases are excited sequentially based on the rotor pole position[8].

Received : 05 January 2022, Revised : 06 October 2022
Accepted : 09 December 2022, Online published : 10 March 2023

The performance (i.e. average torque, torque ripple, efficiency, and power density) of an SRM is mainly influenced by the number of phases[9], number of poles on the stator and rotor[10], properties of the core material[11], number of turns per phase[12] and geometric design variables[6-7]. The impact of geometric variables on performance has been documented in research in the past[13-15], but the underlying causes have mostly gone unexplored. This is an observed gap in the conducted review of the existing literature so far. The work presented in this paper bridges this gap by suitably predicting and investigating the changes in the reluctance in different segments of the lamination profile for successive designs through successful FEA simulations and an analytical-based MEC model. Various geometric aspects like the rotor diameter, stator and rotor pole arc angles, and stator and rotor yoke thickness have been analysed based on changes in static characteristics. Following this, the performance parameters namely average torque and torque ripple have been evaluated.

2. THEORETICAL BACKGROUND

2.1 Torque Output of an SRM

The torque output of an SRM is quantified in terms of the variation in magnetic co-energy (∂W) due to saliency in the design when the rotor traverses to the aligned position from its unaligned position[16]. The shaded area in the flux linkage v/s current graph indicates the magnetic co-energy (∂W_m) (Fig. 1(a)).

The instantaneous torque (T_e) for a constant phase current (I) is given by the expression;

$$T_e = \frac{\partial W}{\partial \theta} \tag{1}$$

This expression indicates the rate of change of co-energy with the angular state of the rotor (θ).

2.2 Magnetic Equivalent Circuit (MEC) of an SRM

The MEC model can be effectively used to analyse the variation of instantaneous torque with the rotor positions (θ) based on reluctance variation[16]. The reluctance of a flux tube in each segment is portrayed in the form of resistance. Magnetic reluctance (R) for any segment in the circuit is given by the expression;

$$R = \frac{l}{\mu_o \mu_r A} \tag{2}$$

where l is the length of the magnetic path, μ_o is the permeability of free space, μ_r is the relative permeability of the magnetic material and A is the area of the cross-section.

The MEC of a flux path Fig. 1b is depicted in Fig. 1c. The equivalent reluctance (R_{eq}) of the circuit can be expressed as;

$$R_{eq} = 2[R_{sp} + R_g + R_{rp}] + \frac{1}{2}[R_{sy} + R_{ry}] \tag{3}$$

It is evident that for any angular position of the rotor, at a constant magnetomotive force (MMF), the flux established in the circuit is dependent on the equivalent reluctance. The description corresponding to the reluctances of the flux path in each segment of the SRM has been tabulated (Table 1).

Table 1. Description of reluctance

Notation	Description
R_{sp}	Reluctance of the stator pole
R_g	Reluctance of the airgap
R_{rp}	Reluctance of the rotor pole
R_{sy}	Reluctance of the stator yoke
R_{ry}	Reluctance of the rotor yoke

The MMF required to build the flux in the circuit is expressed as;

$$MMF = NI = \phi R_{eq} \tag{4}$$

where, NI (product of the number of turns, N, and phase current, I) is the MMF and ϕ is the flux.

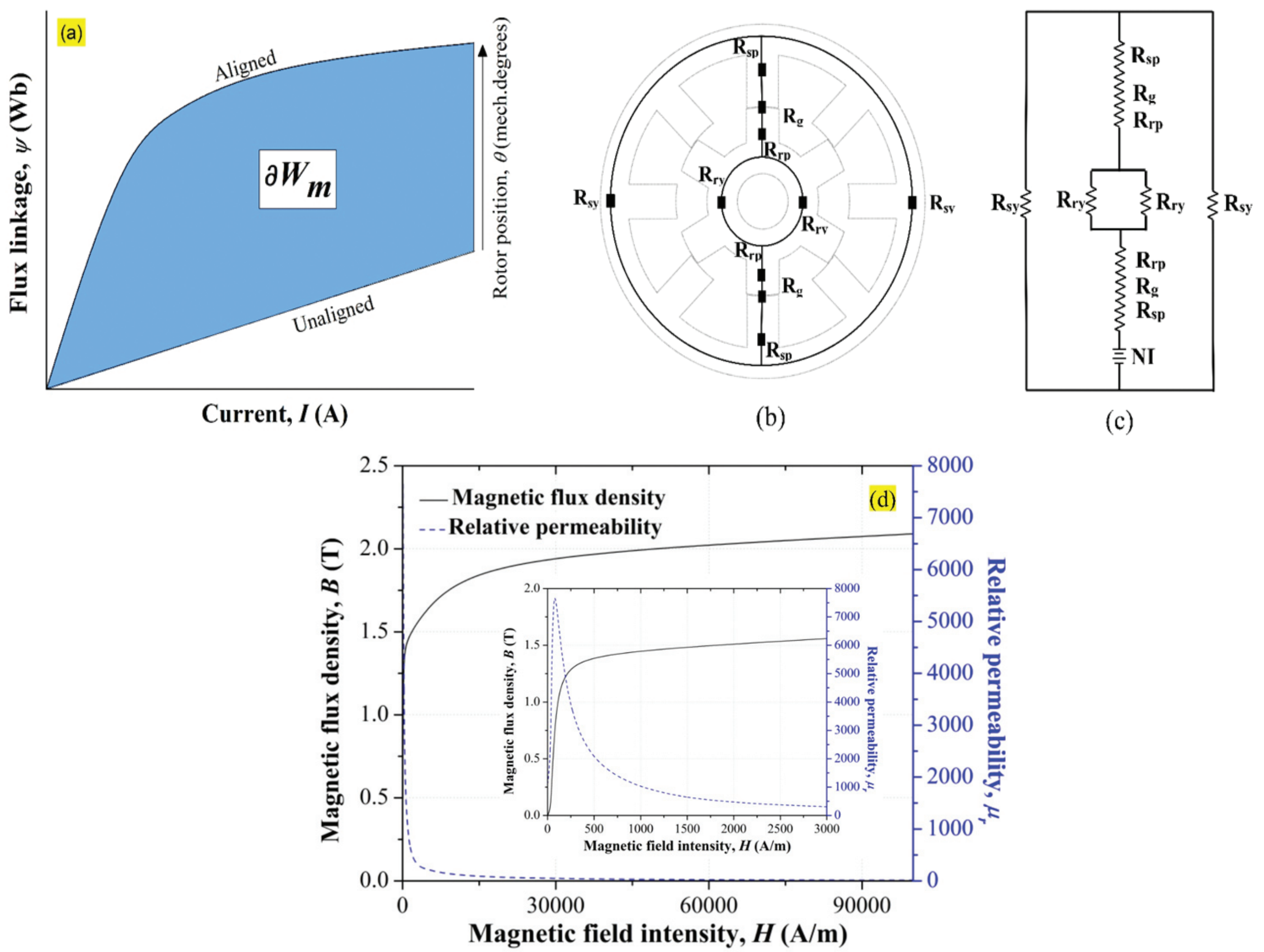

Figure 1. (a) Flux linkage vs current characteristics, (b) Flux path, (c) MEC for the flux path and (d) B-H curve of M270_35A.

2.3 B-H Characteristics of the Core Material

The core material used in the present study is M270_35A (0.35 mm lamination thickness, Fe -96.8 % and Si 3.2 %)[17]. From Fig. 1(d), it is observed that the material offers the least reluctance for operating flux densities in the linear region due to the higher value of relative permeability. Beyond this, it exhibits nonlinear characteristics due to magnetic saturation leading to an increased reluctance owing to a drop in the relative permeability.

3. METHODOLOGY

This study intends to investigate the influence of change in the dimensions of the geometric design variables on the performance of SRM. 2D-FEA was carried out to determine the static characteristics. The reluctance in different segments has been calculated by using the analytical-based MEC model. Based on the results obtained, performance indicators such as average torque and torque ripple are calculated. A four-phase 8/6 inner rotor type SRM configuration (Fig. 2(a)) was used in this study. The notations of each design variable with their respective description have been provided in Table 2. Table 3 shows the entities that have been predetermined.

Table 2. Description of design variables

Notation	Description
D_r	Rotor diameter
h_r	Rotor pole height
b_{ry}	Rotor yoke thickness
β_r	Rotor pole arc angle
β_s	Stator pole arc angle
D_s	Stator outer diameter
D	Stator bore diameter
h_s	Stator pole height
b_{sy}	Stator yoke thickness
g	Airgap

Table 3. Predetermined design entities

Motor design variable	Value	Unit
Number of phases, m	4	-
Number of stator poles, N_s	8	-
Number of rotor poles, N_r	6	-
Stator outer diameter, D_s	160	mm
Stack length, L	40	mm
Peak phase current, I	250	A
Number of turns per phase, N_{ph}	16	-
Airgap, g	0.4	mm
Shaft diameter, D_{sh}	25	mm

3.1 Design of SRM

The procedure for the design of SRM follows those outlined by Miller[9], Krishnan[16], and Bilgin[18]. Based on this, the empirical relations governing each design variable are enlisted as follows.

3.1.1 Rotor Diameter (D_r)

According to Miller[9], the ratio of D_r to the D_s is 0.5~0.55. Based on this, for a fixed D_s of 160 mm, D_r is varied from 80-88 mm with an increment of 2 mm causing a reduction in h_s. Here, β_s=22.5°, β_r=23.5°, $b_{sy}=b_{ry}=0.85\omega_{sp}$, where ω_{sp} is the stator pole width.

3.1.2 Pole arc angles (βs and βr)

(a) Stator pole arc angle (βs)

$$0.4 < \frac{\beta_s}{\theta_{sp}} < 0.5 \tag{5}$$

θ_{sp} is the stator pole pitch (45°). As per the above constraint, β_s is varied from 18 to 23 degrees in steps of 1 degree. Here, D_r = 84mm, $\beta_r=\beta_s+1$ and $b_{sy}=b_{ry}=0.85\omega_{sp}$.

(b) Rotor pole arc angle (βr)

$$1.0 < \frac{\beta_r}{\beta_s} \leq 1.2 \tag{6}$$

β_r is varied from 22.5 to 27 degrees in steps of 1.5 degrees. For each trial, β_s=22.5°, D_r= 84 mm and $b_{sy}=b_{ry}=0.85\omega_{sp}$.

3.1.3 Yoke thicknesses (b_{sy} and b_{ry})

(a) Stator Yoke thickness (b_{sy})

$$\omega_{sy} > b_{sy} \geq 0.5\omega_{sy} \tag{7}$$

b_{sy} varies from 11 to 17 mm with an increment of 1mm. For each trial, β_s=22.5°, β_r=23.5°, D_r= 84 mm and $b_{ry}=0.85\omega_{sp}$.

(b) Rotor Yoke Thickness (bry)

$$b_{ry} \geq 0.5\ \omega_{sp} \tag{8}$$

Based on this, the b_{ry} is increased from 9 to 19 mm with a step size of 2mm. Here, β_s=22.5°, β_r=23.5°, D_r= 84 mm and $b_{sy}= 0.85\omega_{sp}$.

3.2 2D-Finite-Element Analysis

Using the FEA-based ALTAIR FLUX™, a 2D magneto-static simulation is carried out to determine the static characterisation parameters. The geometry of SRM is modeled using AutoCAD and then exported to the FEA software. Following this, a finite number of elements are obtained after discretizing the SRM model (Fig. 2(b)). A fine mesh is employed in the core regions which are prone to magnetic saturation (stator and rotor pole tips) and in the air gap region since the airgap varies with the angular position of the rotor (Fig. 2(c)).

Table 4. Mesh details

Description	Value
Number of nodes	1,87,897
Number of line elements	8075
Number of surface elements	93892
Mesh order	2nd
Number of excellent-quality surface elements	99.92 %
Number of good-quality surface elements	0.08 %
Number of average-quality surface elements	0.01 %
Number of poor-quality surface elements	0 %

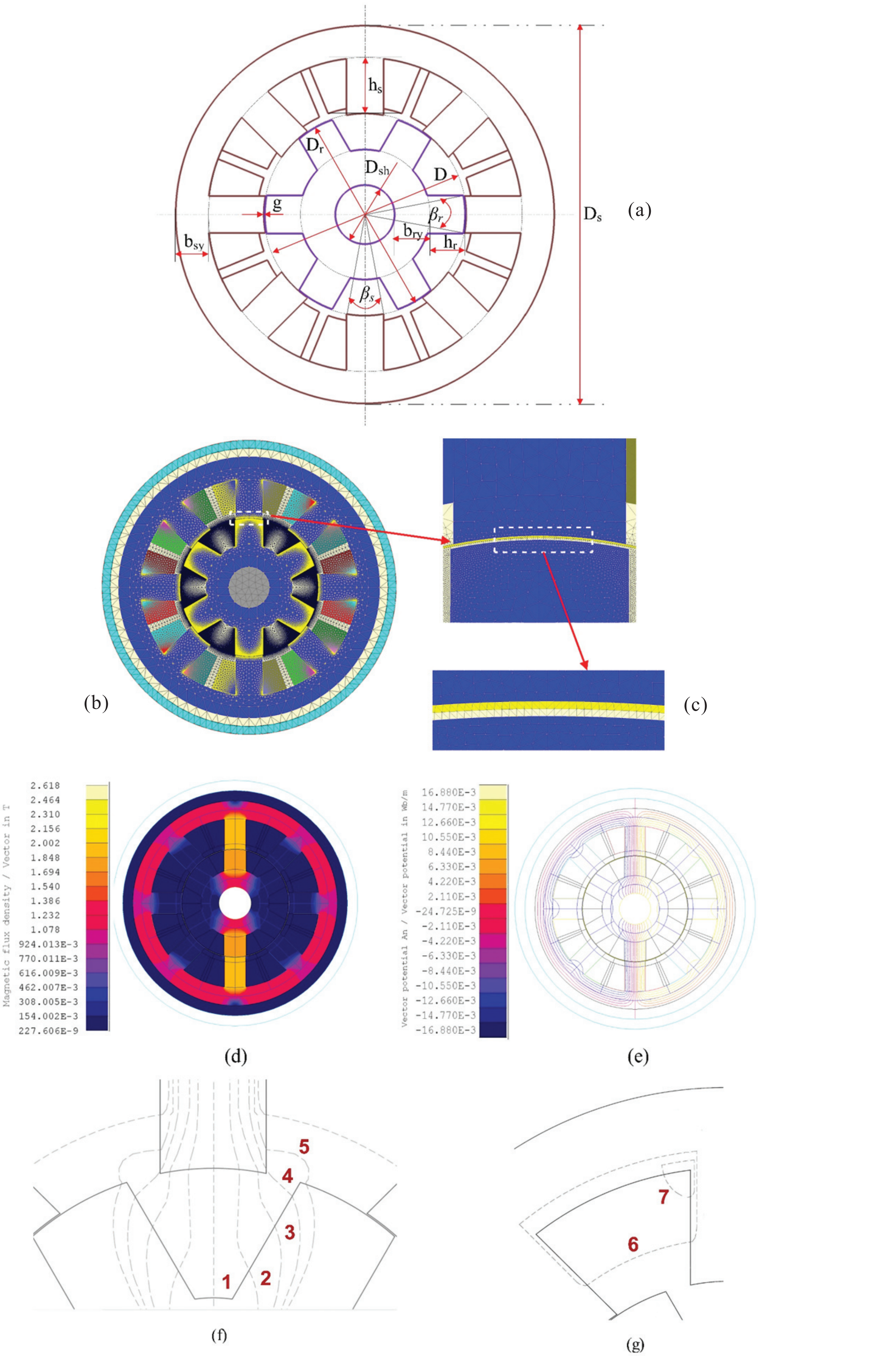

Figure 2. (a) Geometric design variables, (b) and (c) FEA model of the SRM, (d) Flux density plot, (e) Flux paths, (f) and (g) Flux paths at the unaligned position.

In regions away from the airgap, a coarse mesh is employed. A total of 93982 second-order triangular elements were used in the finite element model. The mesh in all the regions of the model was created using the same element type. The quality criteria of the triangular surface elements are based on their smallest angle (α). The quality of the element is classified as excellent if α > 30°, good if α € (15°, 22.5°), average if α € [22.5°, 30°], and low if α € [0°, 15°][19]. Details of the mesh for one of the simulations conducted have been mentioned in Table 4.

The non-linear Poisson's equation governing the 2D magneto-static field problem in the x, y coordinates is expressed as[20];

$$\frac{\partial}{\partial x}\left(\gamma\frac{\partial A_z}{\partial x}\right)+\frac{\partial}{\partial y}\left(\gamma\frac{\partial A_z}{\partial y}\right)=-J_z \tag{9}$$

Where, J_z corresponds to the current density comprising the component normal to the plane (x,y), A_z is the magnetic vector potential in the z-axis and γ is the magnetic reluctivity. The value of magnetic vector potential at the outer circumference of the SRM (homogenous Dirichlet's boundary condition) is fixed to zero (A_z=0). Also, the distribution of the magnetic field in the axial direction of the SRM within the motor is constant.

Equation 9 is solved to determine the magnetic vector potential at each of the element nodes. Electromagnetic quantities namely torque, flux linkage, and flux density are then post-processed from the calculated magnetic vector potentials. In this study, the FEA model is solved to determine the static characteristics for 30 mechanical degrees (unaligned to aligned rotor position) with the phase being energised with a constant MMF of 4000 AT (N = 16 and I = 250 A). The magnetic flux density plot and the flux paths in the aligned position obtained from FEA are shown in Fig. 2(d) and Fig. 2(e) respectively.

3.3 MEC Model

The reluctance in different segments of the motor in both the unaligned (θ = 0°) and aligned positions (θ = 30°) is calculated at 250 A using the MEC model[16] in MATLAB R2020b. In the present model, 7 flux paths have been considered (Fig. 2f and Fig. 2g). For the unaligned position, the process is initiated by assessing a flux path with an assumption of an elementary value of flux density at the stator pole (B_{sp}). Using this, flux densities are evaluated at different segments. Ampere's circuital equation is applied and expressed as;

$$F_1 = N_{ph}I = \Sigma Hl \tag{10}$$

Where $N_{ph}I$ is the applied MMF and ΣHl is the computed total MMF. The resultant error ensuing between applied (F_1) and calculated MMF (T_{MMF}) is given as:

$$\Delta F = F_1 - T_{MMF} \tag{11}$$

To reduce the error (ΔF) to a minimum value, B_{sp} is reconsidered. Based on this, R_{eq} is calculated (Eqn. 3). Further, the inductance is calculated using Eqn. 12.

$$L=\frac{N_{ph}^2}{R_{eq}} \tag{12}$$

Similarly, the inductances corresponding to other flux paths are calculated and summed to obtain the total inductance. The procedure is repeated for the aligned position.

3.4 Performance Indicators

Based on the static characteristics obtained, the following performance indicators have been calculated;

3.4.1 Average Torque (T_{avg})

The average torque for one revolution is calculated using the expression[9];

$$T_{avg}=\frac{mN_r}{2\pi}\partial W_m \tag{13}$$

In this study since m and N_r are both constant, T_{avg} is a function of the magnetic co-energy (∂W_m).

3.4.2 Torque Ripple (T_{ripple})

The torque ripple is calculated using the expression[21];

$$T_{ripple}=\frac{T_{\max}-T_{\min}}{T_{average}} \tag{14}$$

T_{max}, $T_{average,}$ and T_{min} are the maximum, average, and minimum torques respectively corresponding to the best 15 degrees in the static torque characteristics. While considering the static torque profile for an 8/6 SRM design, of the 30 mechanical degrees, a single phase is theoretically energised for only 15 mechanical degrees. Hence, these best 15 mechanical degrees around the T_{max} ought to be approximately constant to maximize $T_{average}$ and thereby minimize T_{ripple}.

4. RESULTS AND DISCUSSION

A correlation between FEA and MEC model was established following which the static torque characteristics for a given change in design were obtained using FEA. The resulting differences are explained by investigating the reluctances in each segment of the motor. Subsequently, the performance indicators are calculated.

4.1 Correlation Between FEA and MEC Model

The correctness of the developed model is depicted by comparing the inductance values at the unaligned and aligned rotor positions for one of the designs. The results are tabulated in Table 5. A good correlation was found to exist between FEA and the MEC model with an error of about 4 %.

Table 5. Inductance (mH) comparison

θ (°)	FEA	MEC
0	0.0313	0.0326
30	0.0807	0.0832

4.2 Influence of Geometric Design Variables on the Performance Indicators

4.2.1 Rotor Diameter (D_r)

With an increase in D_r, the instantaneous torque (Fig. 3a) was found to increase. The difference in torques was more enhanced at and beyond 7° (i.e. start of overlap between the stator and rotor pole corners). This is evident from the co-

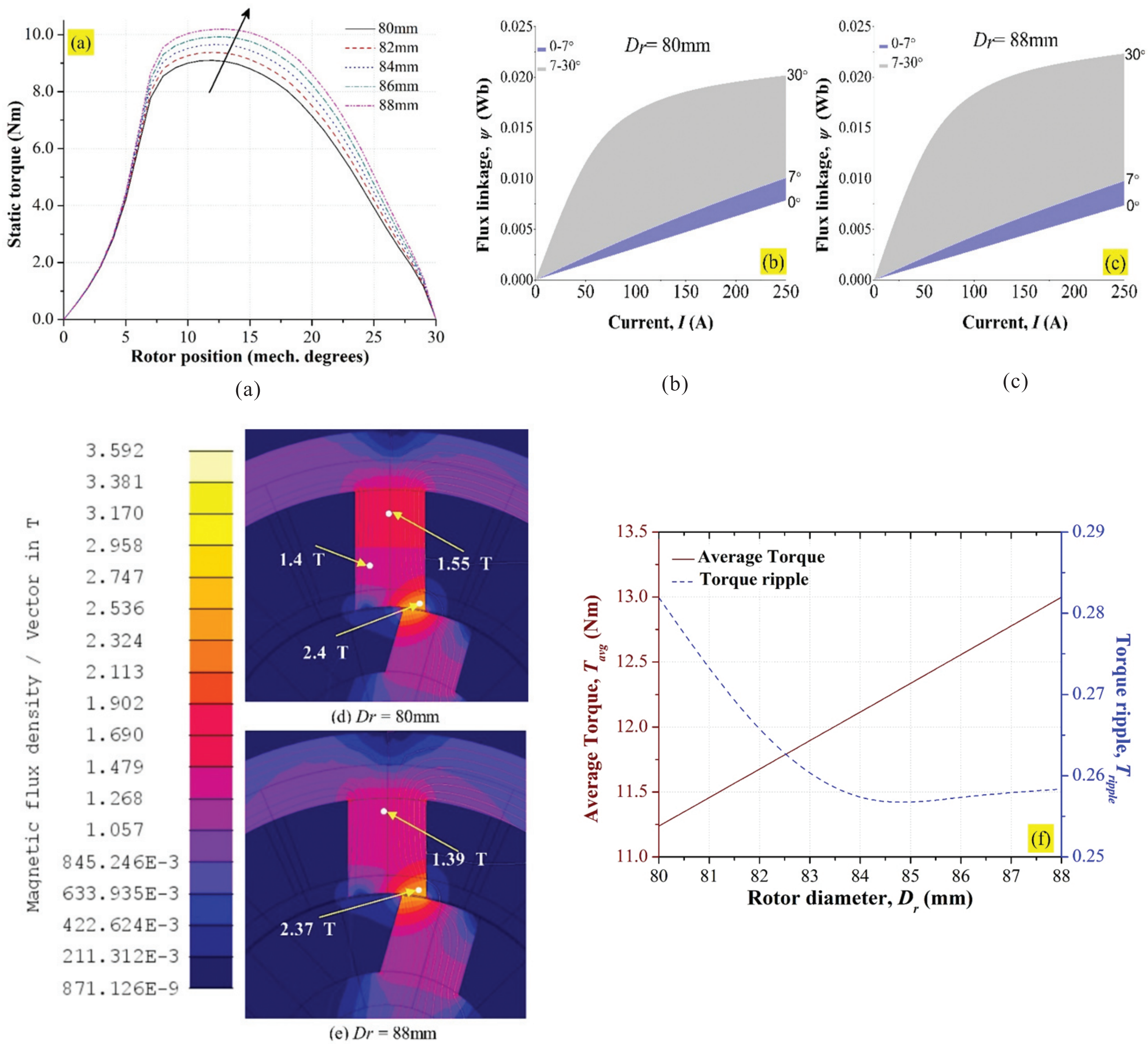

(a) (b) (c)

(e) (f)

Figure 3. Influence of change in D_r; (a) Static torque profile, (b) and (c) Co-energy comparison between 80 and 88 mm designs (d) and (e) Flux density comparison (f) Average torque and torque ripple.

energy plots of the two extremities of 80 and 88mm (D_r) at 250A (Fig. 3b and Fig. 3c). At and above 7°, the dominance of R_g decreases due to its reduced mean path length and total flux path reluctance constitutes a larger segment of core material[18]. Hence, this scenario necessitates an analysis of R_{sp} which was subject to variation corresponding to a change in D_r. For instance, R_{sp} at 14° was compared to understand the variation of co-energy between 7°-30°. The operating flux densities for the 88mm design were found to be lower than those for 80mm (Fig. 3d and Fig. 3e) in the stator pole signifying an increased relative permeability (Fig. 1d). This in conjunction with a shorter mean length (due to reduced stator pole height) and a higher cross-sectional area (β_s=22.5° in both cases) of the flux path in the stator pole cumulatively decreases R_{sp} (Eqn. 2) and thereby R_{eq}. The above findings are also corroborated by results obtained with the MEC model (Table 6, θ=30°). This augments the available MMF to drive the flux across the airgap thus increasing the rate of co-energy. Hence, the improvement in the instantaneous torque is mainly dictated by R_{sp} whose influence is pronounced between the start and full overlap condition. This caused the co-energy of the 88mm design to be higher than the 80 mm design.

Following this, the performance indicators have been calculated. The increase in D_r resulted in an increase in the average torque (Fig. 3f) due to a higher co-energy which has been detailed in the previous paragraph. Similar findings were also reported by Jiang[7], *et al*.. With an increase in rotor D_r, the torque ripple slightly decreases, which is primarily due to less

Table 6. Reluctance variation with the change in D_r

θ (°)	D_r (mm)	R_{sy} (AT/Wb)	R_{sp} (AT/Wb)	R_g (AT/Wb)	R_{rp} (AT/Wb)	R_{ry} (AT/Wb)	R_{eq} (AT/Wb)
0	80	2900	1900	3921000	500	700	7847000
	88	3200	1800	4181000	600	800	8371000
30	80	40600	**921000**	551200	40600	2400	**3048000**
	88	41000	**788000**	536000	42000	2400	**2754000**

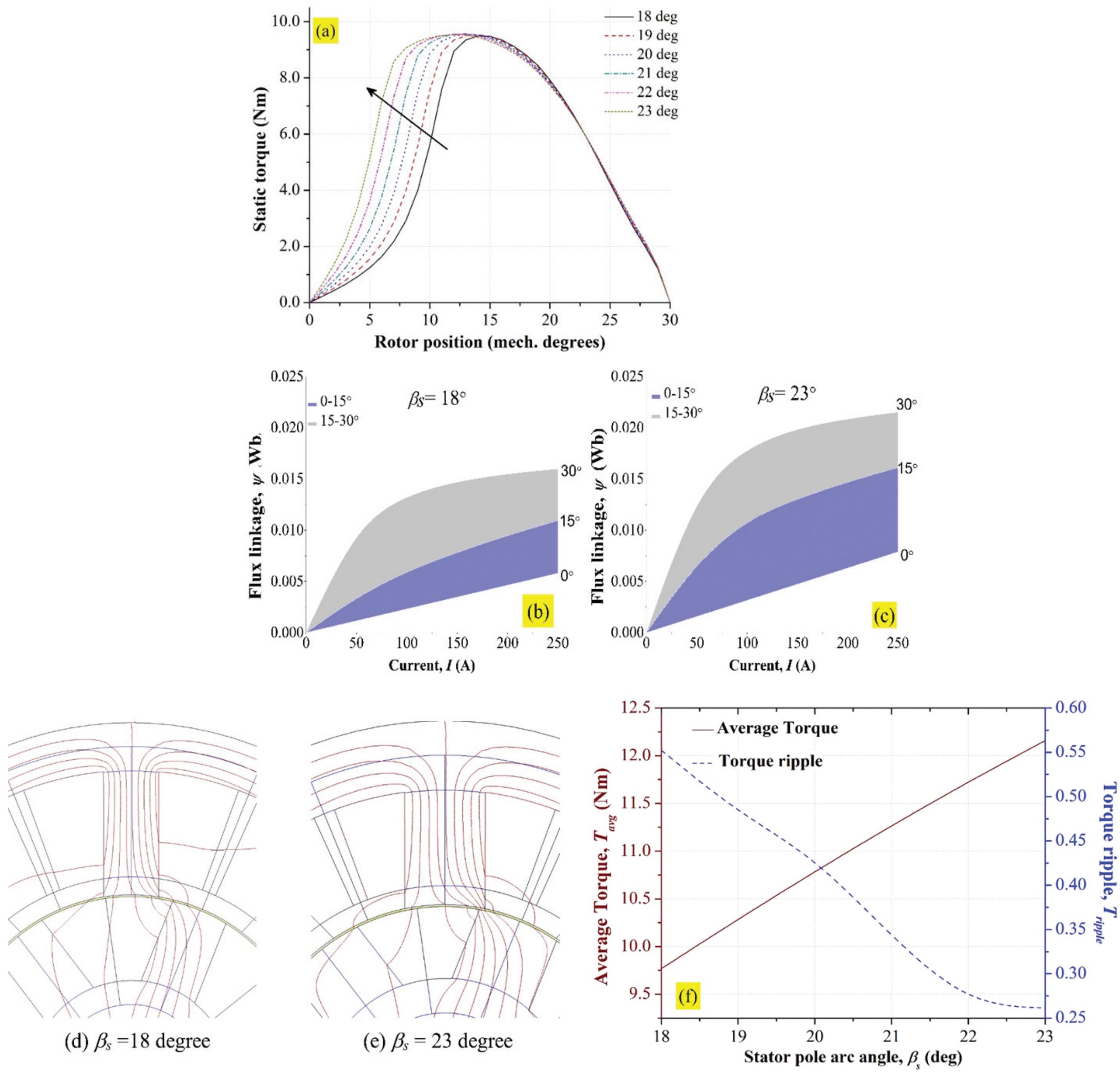

Figure 4. **Influence of change in β_s; (a) Static torque profile, (b) and (c) Co-energy comparison between 18 and 23° designs (d) and (e) Flux paths at 8° rotor position (f) Average torque and torque ripple.**

magnetic saturation in the stator pole for designs with higher D_r. Due to this, designs with higher values of D_r had utilizable 15 mechanical degrees that were broader, which decreased the torque ripple compared to designs with lower values of D_r.

4.2.2 Pole arc Angles

4.2.2.1 Stator Pole arc Angle (β_s)

SRM designs with enlarged β_s have ameliorated instantaneous torque for rotor positions below 15° (Fig. 4a).

Table 7. Reluctance variation with the change in β_s

θ (°)	β_s (°)	R_{sy} (AT/Wb)	R_{sp} (AT/Wb)	R_g (AT/Wb)	R_{rp} (AT/Wb)	R_{ry} (AT/Wb)	R_{eq} (AT/Wb)
0	18	4300	2700	**5306000**	800	1000	**10620000**
	23	2700	1800	**3899000**	500	800	**7806000**
30	18	51900	**1150000**	704500	51900	2600	**3849000**
	23	45100	**833000**	535000	47100	2500	**2855000**

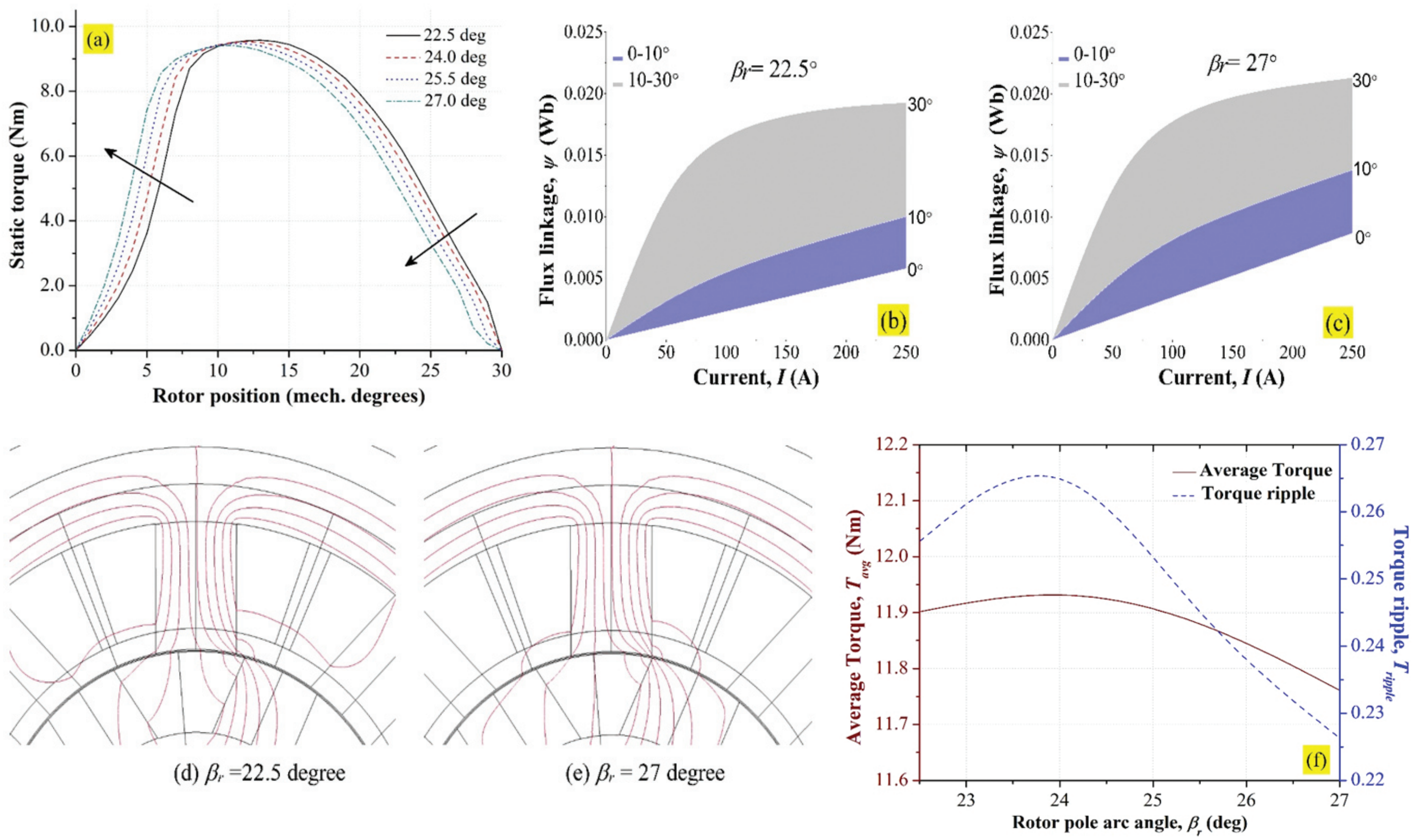

Figure 5. Influence of change in β_r: (a) Static torque profile, (b) and (c) Co-energy comparison between 22.5 and 27° designs, (d) and (e) Flux paths at 5° rotor position and (f) Average torque and torque ripple.

Table 8. Reluctance variation with the change in β_r

θ (°)	β_r (°)	R_{sy} (AT/Wb)	R_{sp} (AT/Wb)	R_g (AT/Wb)	R_{rp} (AT/Wb)	R_{ry} (AT/Wb)	R_{eq} (AT/Wb)
0	22.5	2900	1800	**4135000**	500	700	**8278000**
	27	2600	1700	**3543000**	400	700	**7093000**
30	22.5	31900	854000	564000	**43200**	2400	**2923000**
	27	32000	855000	552000	**15000**	1400	**2886000**

This contrast is apparent in the 18° and 23° β_s designs from their flux linkage characteristics (Fig. 4b and Fig. 4c). The unaligned flux linkage at 250 A was higher in the 23° β_s design in comparison to the former mainly due to a lower value of R_g (Table 7). This can be attributed to the reduced mean length and increased cross-sectional area of the flux path in the air gap caused by the decrease in angular clearance between the rotor and stator pole corners[14]. An instance of this is evident from flux linkage distributions at the 8° rotor position obtained from FEA (Fig. 4d and Fig. 4e). This phenomenon led to an early rise in the static torque, causing an increase in the length of the torque production zone which is noticeable from the static torque profiles of designs with higher β_s (Fig. 4a). This behavior caused an enhancement in the average torque (also observed in the co-energy plots, Fig. 4b, and Fig. 4c and a considerable reduction in the torque ripple (Fig. 4f) which can be ascribed to the best utilizable 15 mechanical degrees during commutation approximating the maximum torque value in the static torque graph.

4.2.2.2 Rotor Pole Arc Angle (β_r)

With enlargement in the β_r, the static torque profiles show

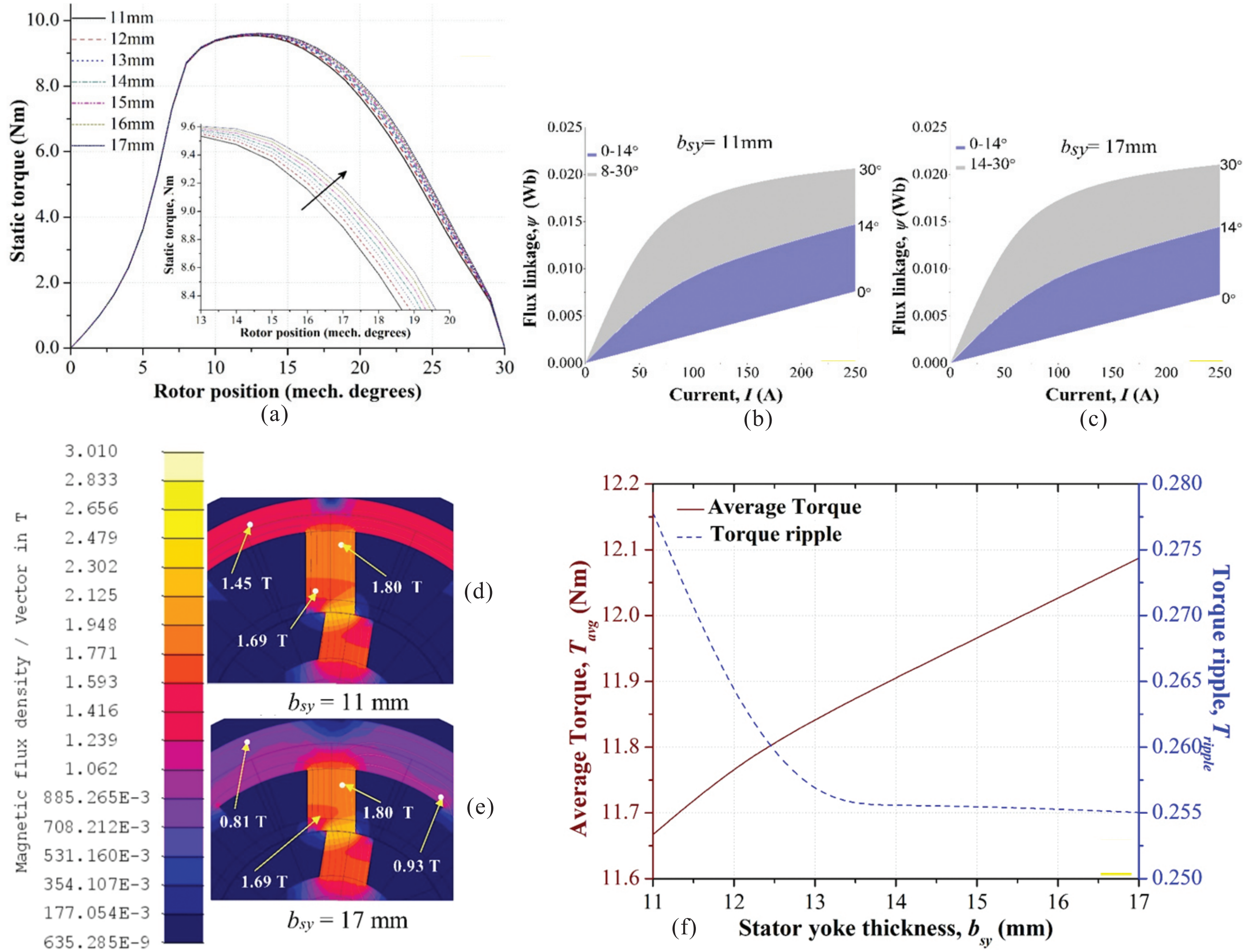

Figure 6. Influence of change in b_{sy}: (a) Static torque profile, (b) and (c) Co-energy comparison between 11 and 17 mm designs (d) and (e) Flux density comparison, (f) Average torque and torque ripple.

Table 9. Reluctance variation with the change in b_{sy}

θ (°)	b_{sy} (mm)	R_{sy} (AT/Wb)	R_{sp} (AT/Wb)	R_{g} (AT/Wb)	R_{rp} (AT/Wb)	R_{ry} (AT/Wb)	R_{eq} (AT/Wb)
0	11	3600	2000	4045000	500	700	8098000
	17	2400	1700	4241000	600	700	8487000
30	11	**49900**	796000	653300	37500	2900	**2999000**
	17	**24700**	781000	649000	38000	2800	**2947000**

quick rise and fall (Fig. 5a). This behavior can be appreciated from the co-energy plots for designs with β_r equalling 22.5° and 27°(Fig. 5b and Fig. 5c). The design with 27° β_r had a higher flux linkage between the rotor position of 0° and 10° than the 22.5° β_r which was vice-versa between 10° and 30°. The former is due to the difference in R_g (due to reduced angular clearance between rotor and stator pole corners) between the designs which is evident from the flux distributions at the 5° rotor position (Fig. 5d and Fig. 5e). Unaligned flux linkage of the 27° design was higher due to decreased R_{eq} which in effect is due to a lower value of R_g (Table 8). Also, its flux linkage for the aligned position was higher owing to lower R_{eq} which is marginally contributed by a lower value of R_{rp}.

Following this, with an increase in β_r, the average torque marginally increased up to 24° and decreased thereafter (Fig. 5f) which was mainly influenced by the reduction in saliency caused by an enhancement of the unaligned flux linkage. From the static torque profiles, it is observed that the 15 mechanical degrees around the maximum torque point to be utilised during commutation is nearly a constant between all the SRM designs with varied β_r. Hence any change in β_r has minimal influence on the torque ripple which can also be deciphered from the graph (Fig. 5f).

4.2.3 Yoke Thicknesses

4.2.3.1 Stator Yoke Thickness (b_{sy})

Static torque characteristics with different b_{sy} have been plotted in Fig. 6a. The instantaneous torques at and below 14° were nearly the same for all the designs. Beyond 14°, designs with higher b_{sy} showcased increased instantaneous torques in contrast to those with lower b_{sy} which can also be demarcated in the co-energy plots (Fig. 6b and Fig. 6c). Designs with 17 mm b_{sy} displayed lower operating flux densities (reduced magnetic saturation) than those with 11 mm at 21° rotor position in the stator yoke segment (Fig. 6d and Fig. 6e) indicating an increased relative permeability. Also the former possesses a shorter mean length and a higher cross-sectional flux path area in the yoke section which collectively decreased R_{sy} (Eqn. 2) and thereby R_{eq}. The results obtained from the MEC model validated the above findings (Table 9). This resulted in increased instantaneous torque above 14° for 17 mm in comparison to the 11 mm b_{sy} design.

Based on this, it was noted that enlarging the b_{sy} enhanced the average torque output (Fig. 6f). Consequently, the designs with higher b_{sy} due to decreased R_{sy} (as explained above) caused the utilizable 15 mechanical degrees in the static torque profile to be as flat as possible near the maximum torque point which resulted in decreased torque ripple. This was in contrast to the designs with lower b_{sy} which displayed higher torque ripple due to increased magnetic saturation in the stator yoke (Fig. 6f). Similar findings were reported by Hoang[22], *et al*..

4.2.3.2 Rotor Yoke Thickness (b_{ry})

An increase in b_{ry} increases the instantaneous torques above the 19° rotor position (Fig. 7a). However, this improvement is marginal and not significant. This is evident from co-energy plots for b_{ry} with 11 and 19mm (Fig. 7b and Fig. 7c). For a given fixed D_r, increase in rotor yoke thickness shortens the height of the rotor pole. This causes a dilution in the flux density from the rotor pole to the yoke (Fig. 7d and Fig. 7e, b_{ry} = 9 mm and 19 mm at 21° rotor position) reducing the reluctance of the segments R_{rp} and R_{ry} and causing an improvement in the instantaneous torques. These observations are also corroborated by the results obtained from the MEC model (Table 10).

Also, with the increase in b_{ry} up to 17 mm the average torque was found to increase followed by a drop (Fig. 7f). For

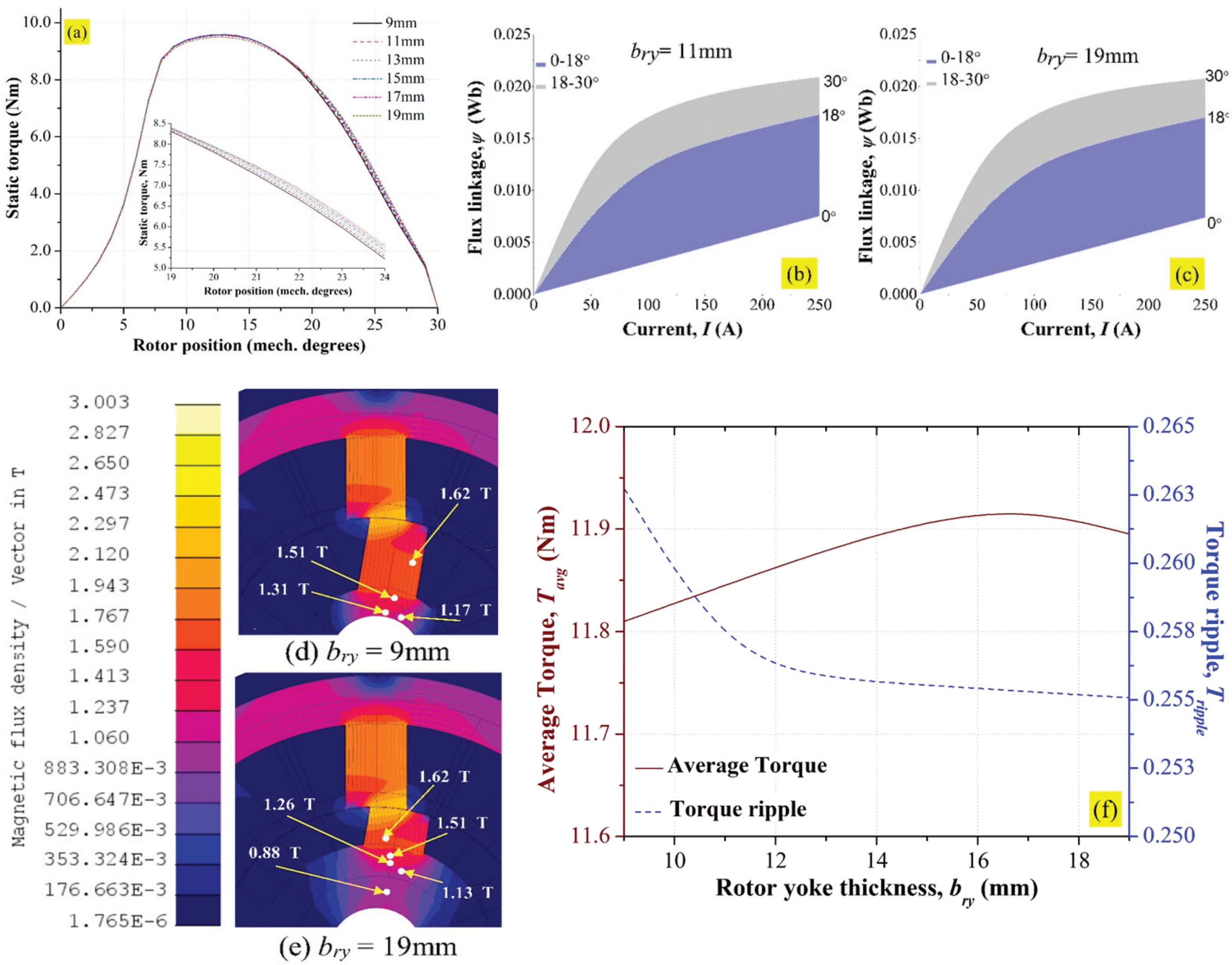

Figure 7. Influence of change in b_{ry}; (a) Static torque profile, (b) and (c) Co-energy comparison between 9 and 19 mm designs (d) and (e) Flux density comparison (f) Average torque and torque ripple.

Table 10. Reluctance variation with the change in b_{ry}

θ (°)	b_{ry} (mm)	R_{sy} (AT/Wb)	R_{sp} (AT/Wb)	R_g (AT/Wb)	R_{rp} (AT/Wb)	R_{ry} (AT/Wb)	R_{eq} (AT/Wb)
0	9	3100	1900	4151000	700	1100	8308000
	19	2500	1700	4012000	400	500	8029000
30	9	42000	855000	565500	**46700**	**3000**	**2958000**
	19	41200	855000	565700	**44800**	**1000**	**2946000**

designs with b_{ry} greater than 17 mm, the increase in unaligned flux linkage impacted the saliency remarkably causing a decrement in average torque. Designs with varied b_{ry} showed minimal effect on the torque ripple since the static torque profiles showed only a marginal change with varied b_{ry} (Fig. 7f).

5. CONCLUSION

A comprehensive parametric study analyzing the influence of geometric design variables on the performance of an SRM was carried out. Key reluctance segments contributing to the change in the static characteristics have been determined using the MEC model. Performance indicators namely average torque and torque ripple were calculated. The following inferences could be drawn from this study:

- A thorough analysis of R_{sp} is necessary while fixing the rotor diameter.
- Pole arc angles majorly influence the rise of static torque profiles due to variations in R_g.
- Average torque improves significantly with an increase in rotor diameter and stator pole arc angle.
- The rise in stator pole arc angle significantly decreases the torque ripple.
- Both average torque and torque ripple are minimally affected by the increase in the rotor pole arc angle and rotor yoke thickness.
- The present work can be extended to study the influence of changing the airgap, tapering of the poles, and providing cut-outs on the rotor core on the performance of the SRM. The key reluctance segments in the SRM responsible for the change can be assessed through the MEC model and FEA simulations discussed here.

REFERENCES

1. Sivakumar, P.; Reginald, R.; Venkatesan, G.; Viswanath, H. & Selvathai, T. Configuration study of hybrid electric power pack for tracked combat vehicles. *Def. Sci. J.*, 2017, **67**(4), 354-59. doi:10.14429/dsj.67.11454.
2. Nishanth, F.; Bohach, G.; Nahin, M.M.; Van de Ven, J. & Severson, E.L. Development of an integrated electro-hydraulic machine to electrify off-highway vehicles. *IEEE Trans. Ind. Appl.*, 2022, **58**(5),6163-74. doi: 10.1109/TIA.2022.3189609.
3. Bilgin, B.; Magne, P.; Malysz, P.; Yinye, Y.; Vera, P.; Matthias, P.; Korobkine, A.; Jiang, W.; Lawford, M. & Emadi, A. Making the case for electrified transportation. *IEEE Trans. Transp. Electrif.*, 2015, **1**(1), 4-17. doi:10.1109/TTE.2015.2437338.
4. Ehsani, M.; Rahman, K.M. & Toliyat, H.A. Propulsion system design of electric and hybrid vehicles. *IEEE Trans. Ind. Electron.*, 1997, **44**(1), 19-27. doi:10.1109/41.557495.
5. Husain, I. Minimization of torque ripple in SRM drives. *IEEE Trans. Ind. Electron.*, 2002, **49**(1), 28-39. doi:10.1109/41.982245.
6. Howey, B.; Bilgin, B. & Emadi, A. Design of an external-rotor direct drive e-bike switched reluctance motor. *IEEE Trans. Veh. Technol.*, 2020, **69**(3), 2552-62. doi:10.1109/TVT.2020.2965943.
7. Jiang, J.W.; Bilgin, B. & Emadi, A. Three-phase 24/16 switched reluctance machine for a hybrid electric powertrain. *IEEE Trans. Transp. Electrif.*, 2017, **3**(1), 76-85. doi:10.1109/TTE.2017.2664778.
8. Srinivasan, S.; Manikandan, S.; Govindaswamy, D. & Ravichandran, K. A Modulation technique for sensorless control of switched reluctance motor. *Def. Sci. J.*, 2019, **69**(3), 223-9. doi:10.14429/dsj.69.14409.
9. Miller, T.J.E. Switched reluctance motors and their control. Magna physics publishing and Clarendon Press, Oxford, 1993.
10. Desai, P.C.; Krishnamurthy, M.; Schofield, N. & Emadi, A. Novel switched reluctance machine configuration with higher number of rotor poles than stator poles: Concept to implementation. *IEEE Trans. Ind. Electron.*, 2009, **57**(2), 649-59. doi:10.1109/TIE.2009.2034678.
11 Li, L.J.; Li, S.H.; Li, G.M.; Li, D.R. & Lu, Z.C. Design and performance prediction of switched reluctance motor with amorphous cores. *Mater. Res. Innovations*, 2015, **19** (sup3), S28-32. doi:10.1179/1432891715Z.0000000001421.
12. Schofield, N.; Long, S.A.; Howe, D. & McClelland, M. Design of a switched reluctance machine for extended speed operation. *IEEE Trans. Ind. Appl.*, 2009, **45**(1), 116-22. doi.org/10.1109/TIA.2008.2009506.
13. Bienkowski, K.; Szczypior, J.; Bucki, B.; Biernat, A. & Rogalski, A. Influence of geometrical parameters of Switched Reluctance Motor on electromagnetic torque. *In* Proceedings of XVI International Conference of Electrical Machines (ICEMS), Lodz, Poland, 2004.
14. Mamede, A.C.F.; Camacho, J.R. & Araújo, R.E. Influence of geometric dimensions on the performance of switched reluctance machine. *Machines*, 2019, **7**(4), 71. doi:10.3390/machines7040071.
15. Smaka, S.; Cosovic, M. & Masic, S. The effects of magnetic circuit geometry on torque generation of

8/14 switched reluctance machine. *In* Proceedings of IEEE XXIV International Conference on Information, Communication and Automation Technologies (ICAT), Sarajevo, Bosnia and Herzegovina, 2013. doi:10.1109/ICAT.2013.6684050.

16. Krishnan, R. Switched reluctance motor drives: Modeling, simulation, analysis, design and application. CRC Press, Boca Raton, 2001.
17. Koželj, P.; Vrtnik, S.; Jelen, A.; Krnel, M.; Gačnik, D.; Dražić, G.; Meden, A.; Wencka, M.; Jezeršek, D.; Leskovec, J. & Maiti, S. Discovery of a FeCoNiPdCu high-entropy alloy with excellent magnetic softness. *Adv. Eng. Mater.*, 2019, **21**(5),1801055. doi: 10.1002/adem.201801055.
18. Bilgin, B., Jiang, J.W. & Emadi, A. Switched reluctance motor drives: fundamentals to applications. CRC Press, Boca Raton, 2019.
19. Altair Flux, Package for electromagnetic and thermal analysis using finite elements FLUX 2D and FLUX 3D, Version 2021, Bangalore, India. https://www.altair.com/flux/. (Accessed on 20 December 2021)
20. Bianchi, N. Electrical machine analysis using finite elements. CRC press, Boca Raton, 2017.
21. Sheth, N.K. & Rajagopal, K.R. Optimum pole arcs for a switched reluctance motor for higher torque with reduced ripple. *IEEE Trans. Magn.*, 2003*,* **39**(5), 3214-6. doi:10.1109/TMAG.2003.816151.
22. Hoang, E.; Multon, B.; Fos, R.V. & Geoffroy, M. Influence of stator yoke thickness and stator teeth shape upon ripple and average torque of switched reluctance motors. *In* Symposium SPEEDAM, Taormina, Italy, June 1994. pp.145-9.

ACKNOWLEDGMENT

The research work was conducted at Centre for System Design (CSD): A Centre of Excellence (https://csd.nitk.ac.in/) at National Institute of Technology Karnataka, Surathkal, with the support from Ministry of Heavy Industries, Government of India under the project 'Switched Reluctance Motor for 2W and 3W' on the Technology platform for Electrical Mobility (TPEM) and Faster Adoption of Electric vehicles (FAME) – India scheme [Grant no – F.No. 3(5)/2018-NAB-II(AUTO) (20331)]. The authors would like to thank the industrial partner of this project M/s Aditya Auto Products and Engineering (I) Private Limited, Bangalore.

CONTRIBUTORS

Mr Sandesh Bhaktha obtained his M. Tech. degree in Manufacturing Engineering and Technology from Manipal Institute of Technology, Manipal in 2017 and currently pursuing his Ph.D. from the National Institute of Technology Karnataka, Surathkal. His research areas include Automotive NVH, Smart materials, Finite element solutions, and Electrical mobility.
His contribution to the present study includes design, execution of FEA simulations and analysis of results and discussions.

Mr Satish Kumawat obtained his M.Tech degree in Mechatronics Engineering from the National Institute of Technology Karnataka, Surathkal in 2021. He is currently working as Control Engineer (R&D) at Siemens Gamesa Renewable Energy, Bangalore. His research areas include Control System Design, Machine Learning and Electrical mobility.
His contribution to the present study includes design, MEC modeling and analysis of results and discussions.

Dr Jeyaraj P. obtained his Ph.D. in Machine Design Section from IIT Madras in 2009. He is currently working as an Associate Professor in the Department of Mechanical Engineering, National Institute of Technology, Surathkal, Karnataka. His research interests include the dynamic behavior of structures under thermal load, vibro-acoustic behavior of composite structures and natural fiber polymer composites.
His contribution to the present study includes the overall supervision, conducting analysis of the results and preparing the manuscript.

Dr K.V. Gangadharan obtained his Ph.D. from IIT, Madras in 2001. Currently working as a Professor in the Department of Mechanical Engineering, National Institute of Technology Surathkal, Karnataka. His areas of research are system design, vibration and its control, smart material and its applications in vibration control, dynamics, finite element analysis, condition monitoring and experimental methods in vibration.
His contribution to the present study includes project guidance, motivation, discussion regarding the results obtained, and preparation of the manuscript.